THESIS FOR THE DEGREE OF LICENTIATE OF ENGINEERING

Powder Bed Fusion – Laser Beam of a non-weldable Ni-base superalloy: Role of process parameters and scan strategies

AHMED FARDAN JABIR HUSSAIN

Department of Industrial and Materials Science

CHALMERS UNIVERSITY OF TECHNOLOGY

Gothenburg, Sweden 2024

Powder Bed Fusion – Laser Beam of a non-weldable Ni-base superalloy: Role of process parameters and scan strategies

AHMED FARDAN JABIR HUSSAIN

Cover:

Site-specific microstructure tailoring represented by EBSD orientation maps in IPF representation. The text 'CAM^2' utilized the standard process and the remainder of the sample used the modified process.

Powder Bed Fusion – Laser Beam of a non-weldable Ni-base superalloy: Role of process parameters and scan strategies

Ahmed Fardan Jabir Hussain

Department of Industrial and Materials Science

Chalmers University of Technology

Abstract

Additive Manufacturing (AM), in particular, Powder Bed Fusion – Laser Beam (PBF-LB) has garnered attention due to its design freedom, near net shape capability, and reduced lead time. Ni-base superalloys are a class of materials used for high temperature applications and widely utilized in the energy and aerospace sectors. However, only a limited number of Ni-base superalloys can be manufactured defect-free through the PBF-LB process. This is especially true for non-weldable Ni-base superalloys such as CM247LC which are susceptible to hot cracking and solid-state cracking. This is an issue that needs to be addressed for increased utilization of these alloys to manufacture complex components by PBF-LB.

This thesis explores strategies that can enable PBF-LB processing of CM247LC with minimal or no hot cracking (solidification cracking) and low residual stresses. The first part of the thesis explores the impact of main process parameters such as laser power, speed, and hatch spacing on solidification cracking, microstructure, and residual stresses. The results from the first part indicate that low solidification cracks are achieved for low line energy density (ratio of laser power and speed) and low hatch spacing. This is due to the shallower melt pools achieved and its effect on solidification structure and in turn grain morphology/texture. The residual stresses are found to be proportional to the volumetric energy density. The second part of the thesis explores the impact of scan strategies on solidification cracking, microstructure, and residual stresses. This was done as the results from the first part of the thesis indicated that the solidification cracking and residual stresses could not be reduced solely by optimizing laser power, speed, and hatch. Therefore, the study varied the stripe width with optimized laser parameters. The results seemed to be promising for a short stripe width of 0.2 mm that gave lower solidification cracking and residual stresses. The decrease in solidification cracking has been attributed to the modification in melt pool size/shape and the mushy zone length. The lower residual stresses were possibly caused by the increased re-melting which led to residual stress relief.

The results from the thesis provide an improved understanding of solidification cracking and residual stress mechanisms in non-weldable Ni-base superalloys manufactured by PBF-LB. The presented results can enable PBF-LB processing of alloys susceptible to hot and solid-state cracking.

Keywords: Ni-base superalloy, non-weldable superalloy, powder bed fusion – laser beam, CM247LC, scan strategy, residual stresses, solidification cracking.

Preface

The work presented in this licentiate thesis was conducted at the Department of Industrial and Materials Science at Chalmers University of Technology between December 2021 and April 2024. The work has been carried out under the supervision of Professor Eduard Hryha and Adjunct Professor Håkan Brodin (Siemens Energy AB). This work was conducted within the framework of the *Centre for Additive Manufacture-Metal* (CAM^2) and the project "*Materials for green hydrogen fueled gas turbines through additive manufacturing*" (MAGDA), both supported by the Swedish Governmental Agency for Innovation Systems (VINNOVA).

List of Appended Publications:

Paper I   **Fine-Tuning Melt Pools and Microstructures: Taming Cracks in Powder Bed Fusion – Laser Beam of a non-weldable Ni-base Superalloy**

A. Fardan, A. Fazi, R. Peng, T. Mishurova, M. Thuvander, G. Bruno, H. Brodin, E. Hryha

Materialia, Vol 102059, 2024, https://doi.org/10.1016/j.mtla.2024.102059

Paper II   **Microstructure tailoring for crack mitigation in CM247LC manufactured by powder bed fusion – laser beam**

A. Fardan, A. Fazi, J. Schröder, T. Mishurova, T. Deckers, G. Bruno, M. Thuvander, A. Markström, H. Brodin, E. Hryha

Submitted for publication

Contribution to Appended Publications:

Paper I   The author planned and performed most of the experimental work except for the residual stress measurements, X-ray computed tomography, and Atom Probe Tomography. Analysis of results was performed in collaboration with the co-authors. The author wrote the paper in cooperation with the co-authors.

Paper II   The author planned and performed most of the experimental work except for the residual stress measurements and Atom Probe Tomography. Analysis of results was performed in collaboration. The author wrote the paper in cooperation with the co-authors.

Other publications not appended in the thesis:

Paper   **Effect of Part Thickness and Build Angle on the Microstructure, Surface Roughness, and Mechanical Properties of Additively Manufactured IN-939**

A. Fardan, U. Klement, H. Brodin, E. Hryha

Metallurgical and Material Transactions A, Vol 54, 2023,

https://doi.org/10.1007/s11661-022-06940-7

Contents

1. Introduction

1.1. Background

Additive Manufacturing (AM) is a manufacturing process where materials are joined layer-by-layer until the required part is obtained. The layer-by-layer approach aids in manufacturing near-net shape components with complex designs directly from a three-dimensional computer aided design (3D CAD) model. This design freedom coupled with increased material utilization and shortened lead times has made AM a technology of immense interest for several industries. This is reflected in the market share of AM which was estimated to be USD 16.75 billion in 2022 and is forecasted to reach USD 76.16 billion by 2030 [1].

Powder Bed Fusion – Laser Beam (PBF-LB) of metals is one of the AM technologies which has increased attention due to its capabilities for high performance components [2]. The gas turbine industry in particular has utilized PBF-LB to manufacture or repair certain components [3,4]. The design freedom has enabled complex internal cooling channels in a turbine blade that brings several advantages such as an increased lifetime of the blade, reduced cooling air consumption, or allow higher temperature to be achieved, which can increase the engine efficiency [5]. However, the PBF-LB process is limited by the number of materials, in particular alloys used for high temperature applications such as Ni-base superalloys.

Ni-base superalloys can broadly be divided into weldable and non-weldable based on the material's ability to be processed without metallurgical defects. However, they both have their fair share of challenges that limit their adoption and application for PBF-LB. Two main challenges particularly for non-weldable superalloys are micro-cracking and macro-cracking. Micro-cracking occurs during the PBF-LB process due to a large solidification range. In comparison, macro-cracking occurs during the post-processing heat treatment due to the high residual stresses from the PBF-LB process. On the other hand, weldable alloys that can be processed without micro-cracking have inferior mechanical properties than their conventional counterparts. This is mostly caused by the unique microstructure, grain size, and anisotropy caused by the PBF-LB process. This could potentially also be a problem for the non-weldable superalloys.

To sum up, there are challenges in the PBF-LB processing of non-weldable Ni-base superalloys that require a better understanding to tackle them and to fully utilize these alloys for the PBF-LB process.

1.2. Research objectives

The objective of the research is to evaluate the impact of processing parameters and novel scan strategies that could enable non-weldable Ni-base superalloys manufactured through PBF-LB. The objectives can be summarized in the following research questions (RQ):

RQ1: What is the impact of process parameters on microstructure and micro-cracking in non-weldable Ni-base superalloys?

RQ2: How can novel scan strategies enable defect-free processing of non-weldable Ni-base superalloys?

RQ1 is addressed in Paper I and RQ2 is addressed in Paper II.

2. Powder Bed Fusion – Laser Beam (PBF-LB)

Powder Bed Fusion – Laser Beam (PBF-LB) is one of the powder-based additive manufacturing (AM) technologies that enables the manufacturing of three-dimensional components. Due to its high design freedom, it is of immense interest to several industries such as aerospace and biomedical sectors. This section serves as an introduction to the PBF-LB process and covers topics such as the working principle and microstructure evolution along with some challenges of the PBF-LB process.

2.1. Working principle of PBF-LB

A PBF-LB machine typically consists of a laser system, recoater, powder dispenser, powder collector, and the powder bed as shown in Fig. 1. The PBF-LB operation starts with a three-dimensional CAD (computer aided design) file designed on CAD software. The three-dimensional (3-D) CAD file is then converted to an STL geometry file which is then sliced into two-dimensional (2-D) slices called layers. This 2-D layer information is then transferred to the PBF-LB machine. From the layer information, the PBF-LB process begins by applying a thin layer of powder (~20-40 μm) on a build platform. This is done by the powder dispenser moving up and the build platform moving down by a pre-determined distance. This is followed by the recoater depositing the powder from the powder dispenser onto the build platform and any excess powder is pushed to the powder collector. The laser system then selectively scans the powder bed to melt the powder based on the layer information. The process is then repeated until the final part is obtained. This process takes place inside the build chamber with an inert atmosphere (typically argon) to reduce oxidation during the process.

2.2. Process parameters in PBF-LB

There are several process parameters in the PBF-LB process, but the main process parameters that are typically considered for optimization are laser power (P), laser speed (v), hatch spacing (h), and layer thickness (t). Fig. 2 shows a schematic of the PBF-LB process where the main process parameters are highlighted.
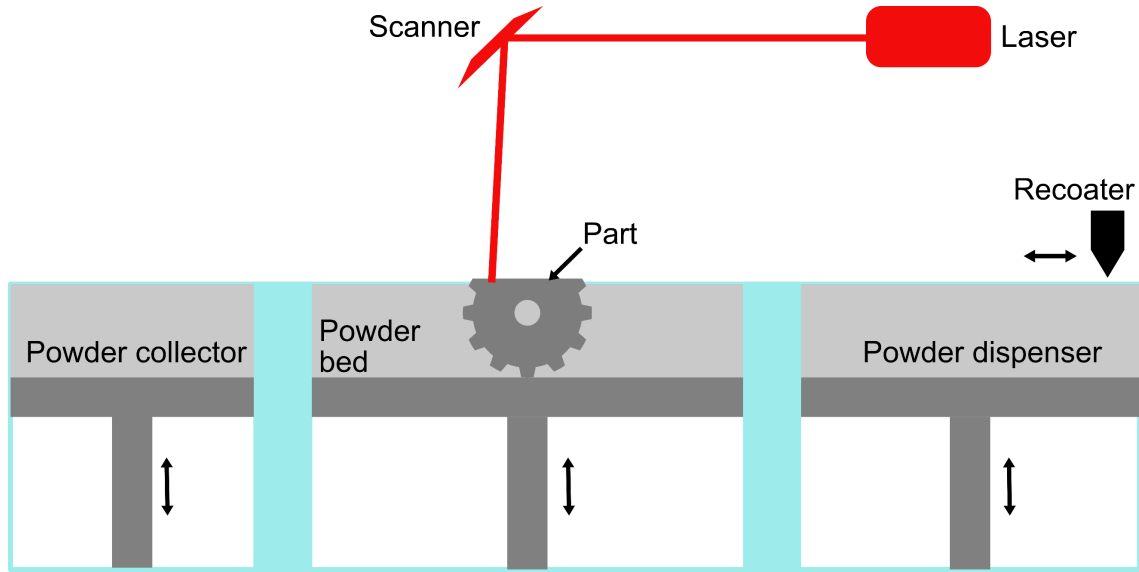
Figure 1. Schematic of the PBF-LB process.

A melt pool forms as the laser scans over a pattern line for a fixed laser power and speed (Fig. 2). This melt pool has a width and depth which is affected predominantly by the laser power and laser speed. For example, higher laser speed for a fixed power can lead to shallower and narrower melt pools. Another important parameter is hatch spacing which is the distance between two adjacent pattern lines. This is also ultimately the distance between two adjacent melt pools. It is important to have sufficient overlap between the adjacent melt pools to avoid the formation of a lack of fusion porosity. Finally, layer thickness is another parameter that determines the amount of material that needs to be melted. A typical layer thickness is about 20 to 40 µm but higher layer thicknesses such as 80 to 120 µm are used for boosting productivity. However, higher layer thickness also leads to lower feature resolution and higher surface roughness. A combined parameter called volumetric energy density (VED) is used to represent the main process parameters, see Eqn. (1).

$$VED \left[{}^{J}\!/_{mm^3} \right] = \frac{P\ [W]}{v\ [{}^{mm}\!/_{s}].\,h\ [mm].\,t[mm]} \tag{1}$$
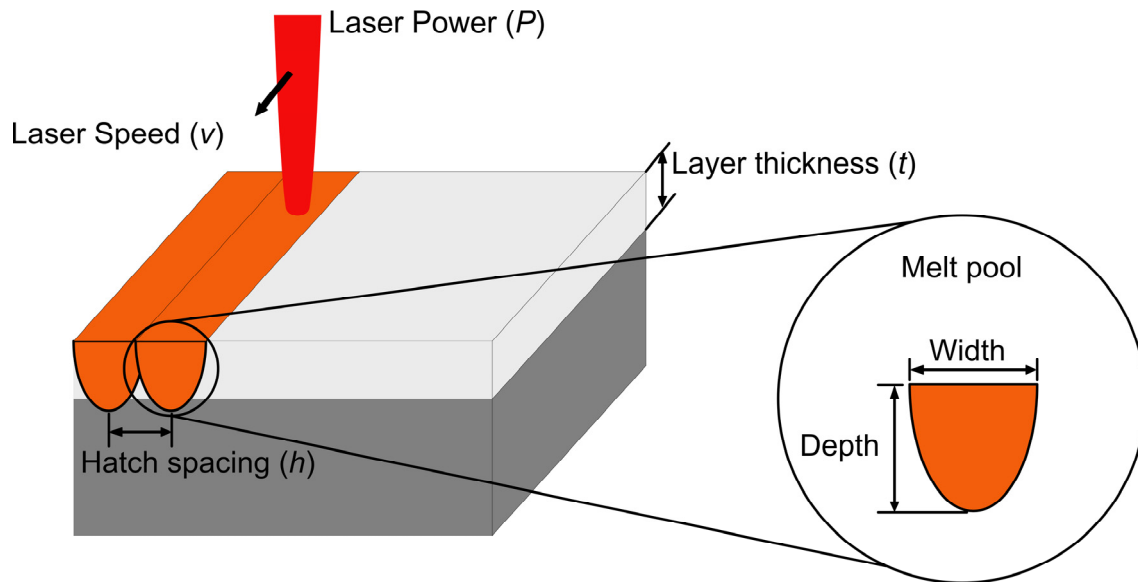
4

Figure 2. Schematic of the printing process in PBF-LB highlighting the main process parameters along with the important melt pool dimensions.

2.3. Scan strategies in PBF-LB

Apart from the laser parameters mentioned above, scan strategy is another crucial parameter. Scan strategy can be referred to as the pattern of the scan vectors that a laser follows in a layer. Additionally, one can also rotate the scan vectors for the following layer. A plethora of scan strategies can be employed for the PBF-LB process and some of the scan strategies are shown in Fig. 3.

The choice of the scan strategy is crucial as it can lead to different microstructures and defect distribution. Using a unidirectional scan strategy can lead to a highly textured microstructure with columnar grains along the build direction. Employing a scan rotation of 90° (Fig. 3d) for successive layers can aid in reducing the anisotropy, lowering residual stresses, and generating a more fine-grained microstructure [6,7]. A stripe scan strategy (Fig. 3f) is commonly used with a scan rotation of 67°. This leads to further reducing anisotropy and breaking down the columnar microstructure [7].

The choice of scan strategy can be crucial for certain alloy systems that are more susceptible to in-process cracking (hot cracking). Certain studies have shown that obtaining fine equiaxed microstructure can reduce hot cracking in superalloys [8,9]. On the other hand, other studies [10] have shown that having a lower fraction of high angle grain boundaries (HAGB) and a higher fraction of low angle grain boundaries (LAGB) is beneficial in minimizing hot cracks as they usually are found in HAGB.

5

In summary, scan strategy is a crucial parameter that could enable defect-free processing with suitable microstructure for intended applications for certain alloys.
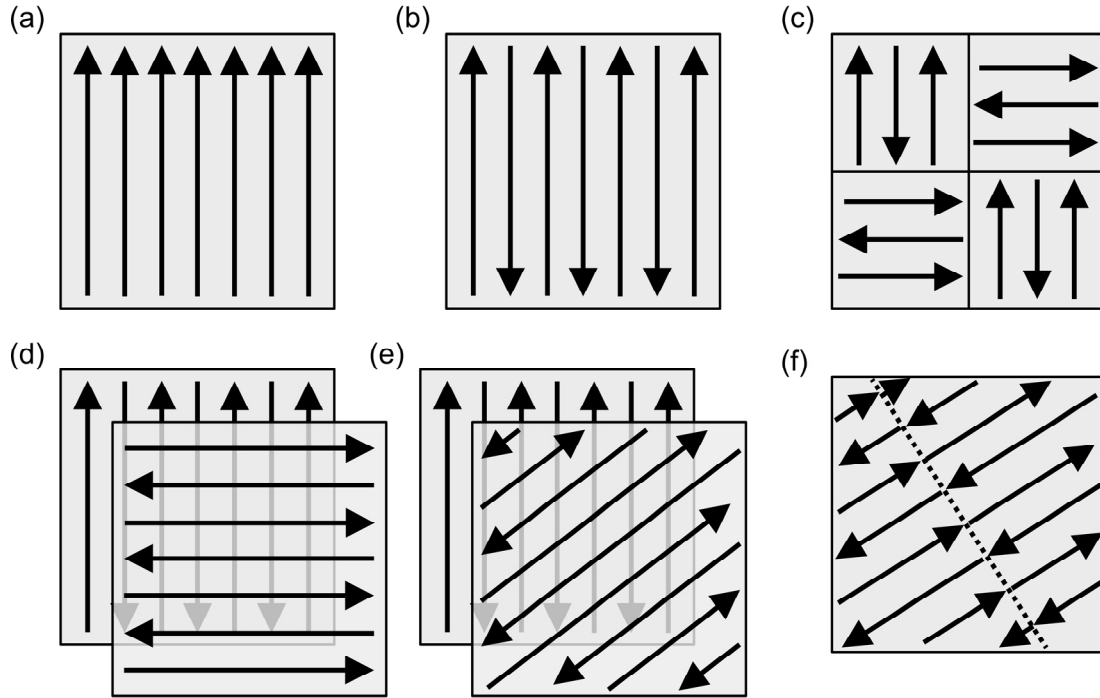

Figure 3. Schematic of selected scan strategies in PBF-LB (a) unidirectional scan strategy, (b) bidirectional scan strategy, (c) chessboard scan strategy, (d) scan rotation of 90° for bidirectional scan strategy, (e) scan rotation of 67° for bidirectional scan strategy (f) stripe scan strategy

2.4. Microstructure evolution in PBF-LB

The rapid melting and solidification of the PBF-LB process leads to unique microstructures. These microstructures are similar to welding rather than casting or forging. This is due to the similar characteristics of PBF-LB and welding where there is a presence of a moving heat source that melts and fuses material causing the presence of a fusion zone and a heat affected zone. Hence, PBF-LB can be considered as a 'multi-pass micro-welding', and a part is manufactured from thousands of melt pools. The temperature gradient and high cooling rate within a melt pool affect the dislocation density, solidification structure, and grain morphology. Furthermore, the elemental segregation is limited to the fine solidification structure. There are possibilities of having different solidification morphologies and this is influenced by the temperature gradient (G) and growth rate (R) as shown in Fig. 4 [11].

When the laser interacts with the metal powder a molten melt pool is formed which then solidifies. The grains formed from the solidifying melt pool are influenced by the underlying

grains from the build plate or previously solidified material. This is called epitaxial grain growth which leads to the formation of columnar grains which can span several layers. The grains are also preferably oriented parallel to the build direction which is the reason for the <100> crystallographic texture mostly observed in face centered cubic (FCC) materials manufactured by PBF-LB.
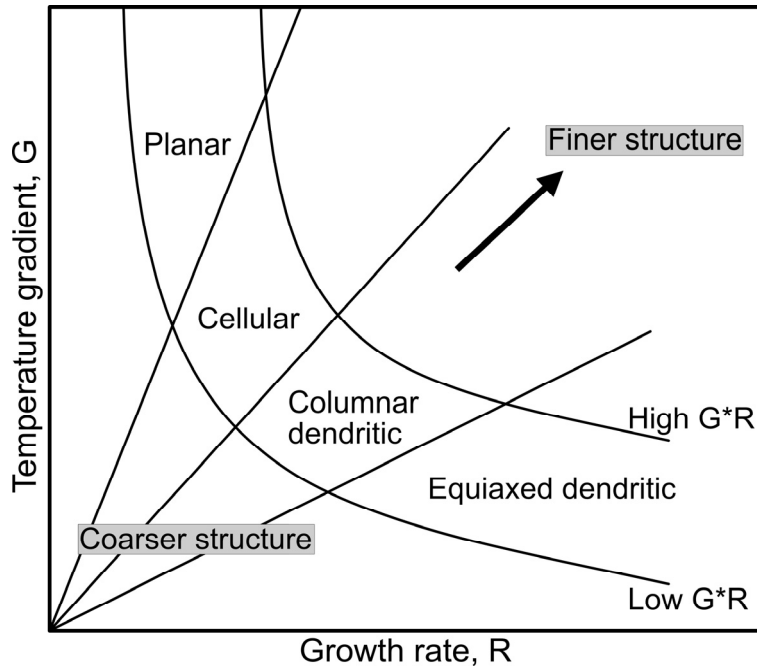

Figure 4. Schematic showing the influence of temperature gradient and growth rate on the solidification mechanism. Adapted from [11].

2.5.   Defects in PBF-LB

Materials produced by PBF-LB can have certain types of defects. These defects are highly influenced by the choice of process parameters for the PBF-LB process. Some of the commonly observed defects in PBF-LB samples are lack of fusion, keyhole, and gas porosity [12] (shown in Fig. 5). Lack of fusion porosity occurs when there is insufficient overlap between adjacent melt pools in the same layer or between layers. This can be mitigated by having sufficient overlap between the melt pools in a layer or between layers. Within a layer, this can be done by reducing the hatch spacing to have sufficient overlaps or by fine-tuning the laser power and speed to have a larger melt pool. Lack of fusion porosity is irregular in shape and has sharp corners which can be detrimental for dynamic loading. Keyhole porosity may form due to the material evaporation and recoil pressure at the bottom of the keyhole. This type of porosity is spherical and can be reduced by increasing the laser speed or reducing the laser power to lower the energy input [13]. Gas porosity is formed from entrapped gas from powder particles in melt

7

pools and is spherical. The gas porosity is typically smaller than the keyhole and is much more random than the keyhole porosity. In addition to the defects mentioned above, microcracks can also occur in certain alloys (Fig. 5c). This type of defect will be covered in detail in Section 3.2.
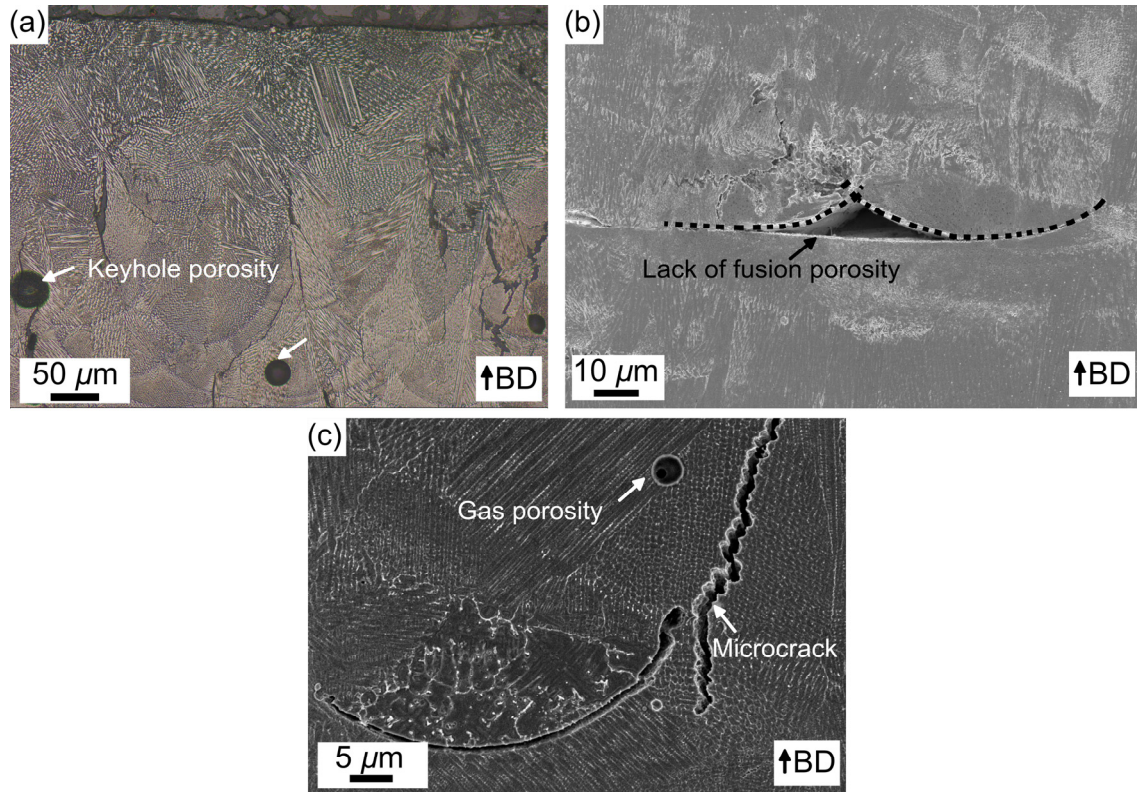

Figure 5. Defects in PBF-LB process. (a) Keyhole porosity, (b) Lack of fusion porosity, (c) Microcrack and gas porosity

3. Superalloys

Superalloys are a class of materials developed for high temperature applications involving high mechanical loads and are required to have high corrosion and oxidation resistance. These alloys have excellent properties at high temperatures and are widely used in gas turbine applications. In fact, the constant drive for gas turbine efficiency has been the driving force for the development and innovations within this material class. Apart from gas turbines, superalloys are also used in rocket engines, nuclear reactors, steam power plants, and petrochemical equipment. Superalloys are further classified into Ni-base, Co-base, and Ni-Fe-base superalloys. This classification is primarily based on the major base element (matrix) used in the alloy [14].

Superalloys can broadly be divided into weldable and non-weldable alloys. This classification is based on the amount of γ' formers (Al and Ti) and is adapted from the weldability diagram by Prager and Shira (Fig. 6a). Although it was developed for welding, it is still applicable to PBF-LB to some extent. Another adaptation of the weldability diagram is shown in Fig. 6b. Here the x-axis contains other γ' formers such as Nb and Ta and this expression is proportional to the predicted γ' equilibrium volume fraction at 700 °C. The y-axis is the Scheil solidification range which can serve as an indication for hot cracking risk.
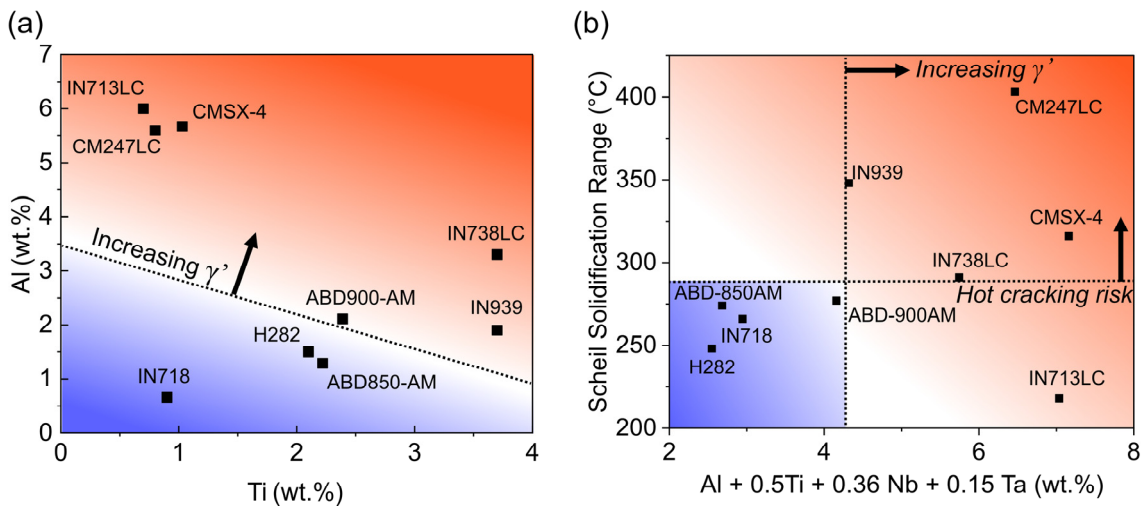
*Figure 6. **(a)** Dependence of weldability (γ' content) on the composition for selected Ni-base superalloys. Adapted from Prager and Shira [15] **(b)** Scheil solidification range versus weldability (γ' content). Adapted from Tang et al. [16]. Al and Ti compositions were obtained for the respective alloys from the following sources: CM247LC [17], IN738LC [18], IN939 [19], H282 [20], IN718 [21], IN713LC [22], CMSX-4 [23], ABD-850AM [16], ABD-900AM [16], MAD542 [24].*

This section would briefly describe the effect of different alloying elements and the cracking mechanisms in superalloys. Furthermore, the specific challenges in PBF-LB of superalloys are also discussed.

3.1. Alloying elements

Superalloys have an FCC crystal structure (γ phase) with different alloying elements. These elements could have multiple beneficial effects such as strengthening (solid solution or precipitate), formation of beneficial phases, or improve certain high temperature properties. For example, Cr is a crucial alloying element added for corrosion and oxidation resistance. Al, Ti, Ta, and Nb are added to form the strengthening precipitate γ' or γ'' (in certain cases). Al is also vital due to the formation of the protective oxide Al_2O_3. Certain elements such as Cr, Al, Co, Mo, W, and Ta also contribute as solid solution strengtheners. C in conjunction with elements such as Cr, Ti, Nb, Mo, Hf, and Ta form carbides (such as MC, $M_{23}C_6$, and M_6C) which also contribute to strengthening. Additions of Hf, B, and Zr have also been found to contribute to grain boundary strengthening and improve high temperature mechanical properties like creep and stress rupture [14].

3.2. Cracking mechanisms in Superalloys

High γ' superalloys are susceptible to cracking either during welding or certain AM processes. The cracking can be broadly divided into hot cracking and solid-state cracking. Hot cracking includes solidification and liquation cracking. This type of cracking occurs during the welding or AM processing. Solid-state cracking occurs during heat treatment of welded or AM components. It is further divided into ductility dip cracking and strain age cracking. These cracking mechanisms were identified and documented in welding and to some extent also apply to the PBF–LB process. It is to be noted that hot cracking has also been observed in certain solid-solution strengthened alloys such as Hastelloy X [25] and Haynes 230 [26].

3.2.1. Solidification cracking

Solidification is an important step in welding or AM process and solidification cracking can occur within a solidifying melt pool. This type of cracking occurs during the last stages of solidification within a melt pool when the liquid film is distributed along the grain boundaries or in the inter-dendritic region. At such a stage the melt pool tends to contract due to the solidification shrinkage and thermal contraction. The surrounding material also contracts but not to the same extent as the melt pool. This leads to the formation of tensile stresses developed across solidifying grains and/or inter-dendritic regions. If the stresses exceed the strength of

the solidified material, then the solidification crack occurs. This type of cracking is characterized by a dendritic morphology surface [27,28].

3.2.2. Liquation cracking

Liquation cracking is a type of hot cracking that occurs due to the local melting of grain boundary constituents in the partially melted zone (PMZ). Liquation cracking sometimes is also referred to as HAZ (heat affected zone) liquation cracking as it occurs at the heat affected zone of a melt pool. Liquation cracking can occur owing to two different mechanisms – the segregation mechanism and the penetration mechanism. On one hand, the segregation mechanism occurs due to the segregation of certain alloying elements (such as S, P and B) to the grain boundaries. This reduces the local melting temperature which is affected by the heat in the HAZ which may lead to the formation of a liquation crack due to the tensile stresses. On the other hand penetration mechanism occurs when secondary phases (eutectic, intermetallics, carbides, etc) do not have enough time for dissolution and can react with the matrix to form a liquid film which under tensile stresses undergoes cracking [28].

3.2.3. Ductility Dip Cracking (DDC)

Ductility dip cracking (DDC) is a form of solid-state cracking reported to occur due to a loss in ductility in superalloys. This loss is known to occur in a temperature range of half of the solidus temperature up to the solidus temperature. The shrinkage strains occurring in and around the weld can lead to the local exhaustion of ductility and lead to DDC [28].

3.2.4. Strain Age Cracking (SAC)

All the cracking mechanisms mentioned until now can occur in both solid-solution and precipitation strengthened superalloys. But strain age cracking (SAC) exclusively occurs in precipitation strengthened superalloy. SAC is a solid-state cracking and occurs during post-processing heat treatment, although it is also possible to occur during reheating of multi-pass welds. This cracking is prevalent in high γ' (Ni_3(Al, Ta, Ti)) precipitation strengthened Ni-base superalloy and is proportional to the Al+Ti content in the alloy. These alloys must be solution annealed before the aging step and it is almost impossible to avoid γ' precipitation due to the high Al+Ti content. So, residual stresses along with stresses caused due to the γ' precipitation lead to strain age cracking. This type of cracking is the main reason for classifying high γ' Ni-base superalloys as 'non-weldable'.

3.3.   Challenges in PBF-LB of Superalloys
3.3.1. Micro-cracking

Certain heritage superalloys with high γ' volume fraction such as IN939 [16,29], IN738LC [30–32] and CM247LC [16,29,33–36] are heavily alloyed and have reported micro-cracking observed in samples produced using PBF-LB. This type of micro-cracking is hot cracking, in particular, solidification cracking that occurs due to the increased solidification intervals. One way of reducing/eliminating solidification cracking is to have an alloy with reduced solidification interval. This means that certain elements have to be removed to reduce the solidification interval and in turn mitigate solidification cracking. For example, some studies have shown that reducing/eliminating elements such as B, Zr and Hf reduced the solidification interval and thus the solidification cracking [32,36]. It is highly possible that the creep properties could be affected as these elements are crucial for grain boundary strengthening [37,38]. There have been attempts to design novel alloys that have eliminated solidification cracking [16,24,39–42], but these alloys need rigorous testing before they can replace the heritage alloys for industrial applications.

Another way is to optimize the process parameters to minimize solidification cracking. Studies have demonstrated that narrower and shallower melt pools with short hatch spacing lead to less or no cracking in PBF-LB [17,43]. This is not unique to the PBF-LB process but welding literature has shown welds with low depth-to-width ratio to be beneficial [27]. This has been attributed to the reduction in the solidification stresses and reduced segregation for welding. This probably is valid for PBF-LB as well, however, the solidification structure and in turn grain morphology also play a major role. Minimizing the high angle grain boundaries can minimize the solidification cracking. This can be explained based on the model by Rappaz [44] where high angle grain boundaries are more susceptible to liquid film presence at lower temperatures. Hence, minimizing high angle grain boundaries can lead to lower solidification cracking. Also, other techniques such as build plate pre-heating [45], modified scan strategy [10] and adding grain refiners or nanoparticles [9,26,46] can aid in minimizing solidification cracking. Furthermore, post-processing heat treatments such as hot isostatic pressing (HIP) can heal solidification cracking [47,48].

3.3.2. Residual stresses

Residual stresses are stresses present in a material and are self-balanced without external stresses. The localized energy input, constrained shrinkage, and the complex thermal history induce residual stresses in parts built by the PBF-LB process. These residual stresses are high

and can cause deformation when certain parts are removed from the build plate. Some parts often require stress annealing before they are removed from the build plate. This is true for most of the alloys manufactured by the PBF-LB process, however there is another complication for superalloys. Superalloys with high contents of Al and Ti (Al+Ti > 5 wt.%) readily form γ' when heat treated. The residual stresses along with precipitation stresses cause strain age cracking. Unlike solidification cracking, SAC is a macrocrack that occurs during post-process heat treatment like HIP. This means that the components are rather useless and need to be scrapped. SAC also tends to occur in complex geometries which limit the usage of certain high γ' Ni-base superalloys such as IN738LC and CM247LC.

Previous studies have shown that there are several ways to reduce SAC. Griffiths *et al.* [49] showed that SAC susceptibility was reduced for a modified alloy of CM247LC. This alloy had no Hf and the lower SAC susceptibility was attributed to the lower γ' volume fraction. Another study by Hilal *et al.* [50] showed that SAC was affected by the process parameters for CM247LC. It was shown that components with higher porosity and solidification cracking did not undergo SAC after HIP. This reduced SAC susceptibility was attributed to the solidification cracking acting as a stress-relief mechanism. However, having a higher degree of solidification cracking from the PBF-LB process can be detrimental if the cracks are interconnected and open to the surface which ultimately will not be healed by HIP. This shows that probably the goal should not only be the elimination of solidification cracking but also to lower the residual stress from the PBF-LB process to reduce SAC.

4. Methodology

This section provides a brief overview of the relevant techniques used.

4.1. Material

Gas atomized CM247LC powder with a particle size distribution of d10 = 18.27 μm, d50 = 30.72 μm and d90 = 51.15 μm was supplied by Höganäs AB (Höganäs, Sweden) as feedstock material. The chemical composition of CM247LC as provided by the powder supplier is shown in Table 1. The chemical composition of the printed PBF-LB part was also analyzed and is shown in Table 1. Carbon and oxygen content were measured using combustion and fusion analysis, respectively. The remaining elements were measured using ICP-OES analysis.

Table 1. Chemical composition of the CM247LC powder and the PBF-LB part (wt.%) used in this study.

	Cr	Co	Mo	C	W	Hf	Ta	Ti	Al	Zr	B	Si	O	Ni
Powder	8.0	9.3	0.5	0.06	9.7	1.3	3.2	0.8	5.6	0.009	0.010	0.08	0.01	Bal.
PBF-LB part	8.1	9.1	0.5	0.06	9.5	1.3	3.1	0.8	5.5	0.011	0.019	0.11	0.005	Bal.

4.2. PBF-LB processing

PBF-LB processing was done on an EOS M290 machine (Electro Optical Systems GmbH, Krailling, Germany) located at Chalmers University of Technology. The machine is equipped with a 400W Yb-fibre laser with a maximum power of 400W and a laser spot size of about 100 μm. The laser has a Gaussian energy distribution and is operated in a continuous wave mode. A stripe scan strategy with a stripe width of 5 mm and stripe overlap of 0.12 mm was used in Paper 1. However, the stripe width was varied from 5 to 0.2 mm in Paper 2. In both the papers, scan rotation of 67° was used and build plate pre-heating varied from 25 to 80°C. Laser power, speed, and hatch were varied for process optimization in Paper 1 while the layer thickness was fixed at 30 μm.

4.3. Metallographic preparation

The cross-section parallel to the build direction was used to observe the defects and microstructure. This cross-section provides information across all the layers. The cross-sections were mounted in a conductive bakelite resin and ground using SiC paper 320, 500, 800, 1200, 2000, and 4000 grit-size on a Struers Tegrapol (Roper Technologies, Copenhagen, Denmark). The force for the grinding steps started at 30 N and progressively decreased to 20 N and was carried out for about 1 – 3 min. This was followed by the diamond polishing step using 3 μm and 1 μm. The polishing step using 3 μm was carried out using the MD-Mol cloth

from Struers. This step is crucial as performing this step with other cloths like MD-Dac or MD-Dur can smear defects like cracks. Finally, the 1 μm polishing was carried out on the MD-Nap cloth. At this stage, the samples are suitable for optical microscopy for defect characterization. The samples underwent additional colloidal silica polishing using 0.25 μm (OP-S) on MD-Chem cloth before etching or further characterization such as scanning electron microscopy. The colloidal silica polishing step is crucial as there can be scratches hidden which can be revealed after etching or in scanning electron microscopy. Two types of etching were performed in this thesis. Firstly, electrolytic etching using 10% phosphoric acid was done at voltages of 5-10 V for 10-20 seconds. This etches away from the dendritic core and leaves the interdendritic region. Secondly, swab etching was performed using Kalling's 2 (Waterless Kalling's, 5g $CuCl_2$ + 100 ml 37% HCl + 100 ml ethanol). This etches away the interdendritic region leaving the dendritic core. Samples were typically washed with distilled water and dried using pressured air before microscopy.

4.4. Optical Microscopy and defect characterization

Optical microscopy was performed using Zeiss Axiovision 7. The microscope has a motorized stage that allows to stitch large areas for defect analysis. The micrographs for defect analysis consisted of acquiring images at a magnification of 100X on as-polished samples as shown in [33] and then using ImageJ for defect quantification. The region of interest is cropped and binarized. The 'Analyze Particle' function is then used to exclude border defects and particles smaller than 20 pixels. A circularity between 0 and 0.3 is identified as a crack and a circularity between 0.3 and 1 is identified as porosity. In paper 1, the individual crack length was obtained by manual measurement. In paper 2, the individual crack length was acquired by obtaining the major axis length of the fitted ellipse. The summation of the individual crack length (in mm) divided by the analyzed cross-sectional area (in mm^2) gives the crack density. The porosity is obtained by using the image threshold function of the particles with circularity greater than 0.3. The melt pool measurements (width and depth) were performed on the top layer of the sample etched with Kalling's 2.

4.5. Scanning Electron Microscopy

Scanning Electron Microscopy (SEM) was performed on two SEMs, namely Leo Gemini 1550 SEM and Zeiss Gemini 450. They both have a field emission gun (FEG) source. The microscope has a number of detectors used for different purposes. All the samples underwent colloidal silica polishing before SEM.

4.5.1. Imaging and chemical analysis in SEM

Secondary Electron (SE) detector provides better topographical contrast and is suitable for studying etched microstructures. SE detector also allowed studying the evidence of the solidification structure in the solidification crack surface. Backscattered electron (BSE) detector provides atomic contrast e.g. MC carbides would appear brighter than the matrix. Accelerating voltages used for SE and BSE imaging were typically 20kV unless specifically stated. SE imaging using the Zeiss Gemini 450 SEM was performed with probe currents of ~0.5 to 1 nA.

Energy Dispersive X-ray Spectroscopy (EDS) was used for chemical analysis. Point, line and map features were employed to show the preferential enrichment of elements. Line analysis was found to be suitable for small carbides. This is because the interaction volume is larger and information can come from the surrounding matrix as well. The working distance for EDS acquisition was 8.5 mm.

4.5.2. Electron backscatter diffraction (EBSD)

EBSD is an SEM-based technique that gives crystallographic orientation information of the sample. It is an SEM technique where the sample is tilted to 70° and an EBSD detector is inserted. The EBSD detectors used were Nordlys II detector (Leo Gemini 1550 SEM) and Oxford Symmetry Detector (Zeiss Gemini 450) from Oxford Instruments. Data clean up consisted of removing wild spikes and zero solution removal using 7 nearest neighbors. The analysis of the EBSD data was performed using MTEX open source MTEX toolbox (version 5.9.0) in MATLAB. The working distance for EBSD acquisition was ~15 to 20 mm.

4.5.3. Electron Channeling Contrast Imaging (ECCI)

ECCI is an SEM-based technique that allows imaging defects such as dislocations and stacking faults. ECCI acquisitions were performed on Zeiss Gemini 450 SEM using the BSE detector. The sample preparation was similar to EBSD i.e. colloidal silica polished for about 10 – 20 minutes. The acquisition is performed using a BSE detector with an accelerating voltage of 20 kV, probe current of ~1.5 nA, and working distance of 5 mm. Unlike controlled ECCI (cECCI) this work does not use EBSD orientation information to guide rotation and tilt to achieve channeling conditions [51]. Therefore, the ECCI acquisitions were performed at a 0° tilt angle on a region that appears dark i.e. nearly in channeling conditions. Defects such as dislocations would appear brighter and can be imaged. In addition to the dislocations, there can also be

atomic contrast from other phases such as carbides which will show up in ECCI. ECCI was used in Paper II.

4.6. Thermo-Calc® AM module simulation

The PBF-LB process was simulated using the AM module in Thermo-Calc 2024a. The composition used for the simulation is shown in Table 2. The TCNI12 database was used for Scheil solidification calculations. The calibrated heat source has an absorptivity of 70% and a beam diameter of ~80 μm given by Thermo-Calc. Steady-state calculations (single track) were run for Paper I to show the effect of parameters on the melt pool and mushy zone. Transient calculations (multiple tracks) with a calibrated heat source were run for Paper II to show the impact of stripe width on the melt pool and mushy zone. Additionally, temperature profiles were obtained through the probe function.

5. Summary of appended papers

This section summarizes the results of the appended papers based on the research questions framed in Section 1.

RQ1 is addressed in Paper I. Paper I explores the impact of laser parameters (laser power, speed, and hatch spacing) on microstructure, residual stresses, and cracking. RQ2 is addressed in Paper II. Paper II explores the impact of stripe width as a scan strategy on microstructure, residual stresses, and cracking.

RQ1: What is the impact of process parameters on microstructure and cracking in a non-weldable Ni-base superalloy?

The motivation behind Paper I was to explore the impact of laser power, speed, and hatch spacing on microstructure, residual stresses, and cracking on CM247LC. CM247LC is a high γ' strengthened Ni-base superalloy (with ~60% equilibrium γ' volume fraction) that is classified as non-weldable due to its increased cracking susceptibility.

The results indicate that CM247LC is susceptible to hot cracking (particularly solidification cracking). The line energy density (*LED*), which is the ratio of power and speed, has a profound effect on solidification cracking. Figure 7 shows selected micrographs with varying *LED* and hatch spacing. It can be seen that low *LED* (0.1 J/mm) and low hatch spacing (0.03 mm) are beneficial in minimizing solidification cracking. Melt pool analysis revealed that low *LED* leads to shallower melt pools, leading to a solidification structure nearly parallel to the building direction that minimizes cracking. The grain morphology and texture also revealed that samples processed with low *LED* (0.1 J/mm) and hatch spacing (0.03 mm) had strong <100> crystallographic texture with columnar grains. However, samples processed with high *LED* (0.3 J/mm) and hatch spacing (0.09 mm) had coarser grains.
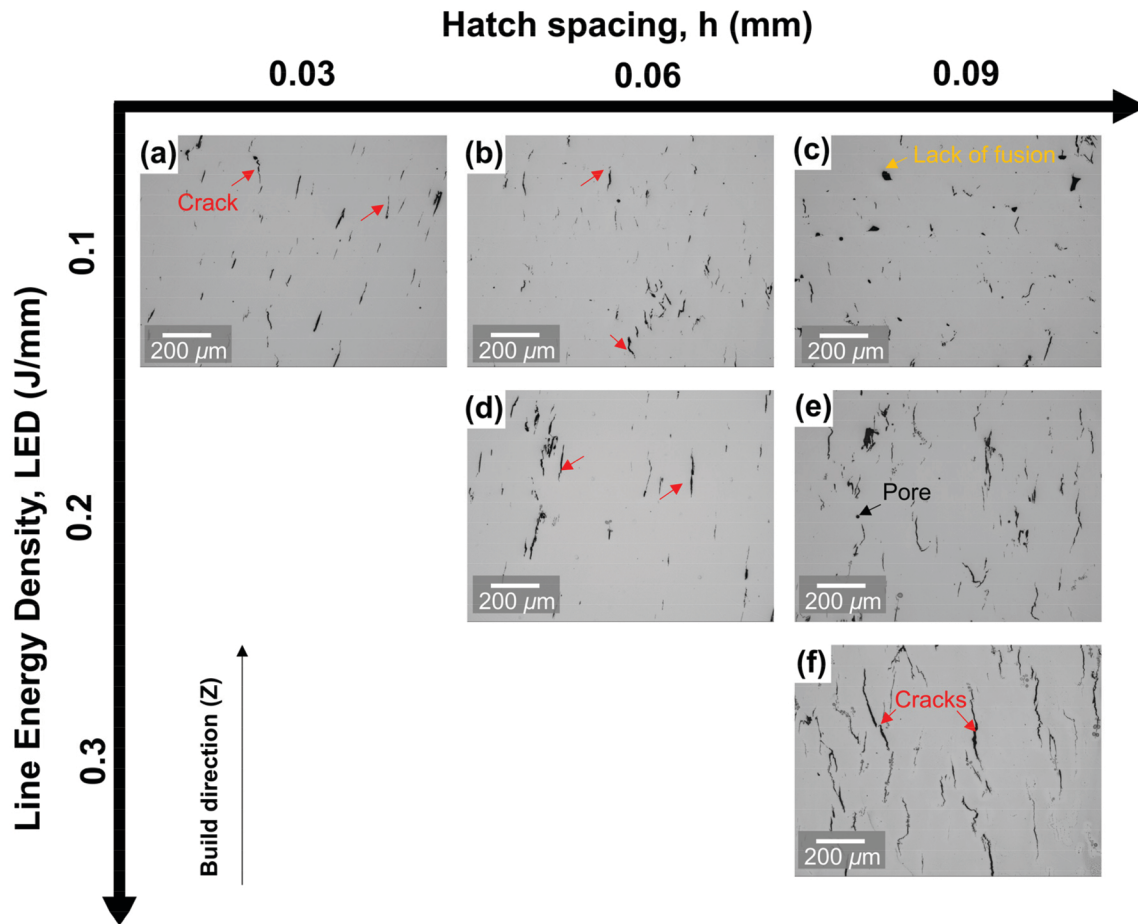
Figure 7. Selected micrographs showing the presence of cracks, pores, and lack of fusion for different LED and hatch spacing. Red arrows in (a), (b), (d) and (f) indicate cracks. Lack of fusion is indicated in (c). A pore is indicated in (e). The empty regions indicate samples that failed during the print [17].

The impact of process parameters on residual stresses was studied. This was done to evaluate the macro-cracking susceptibility of the alloy i.e. strain age cracking. Four samples processed with different *LED* parameters were chosen for residual stress analysis. It is important to note that they had different *VEDs* (Eqn. 1). Two of the samples had completely different parameters but the same *VED*. The results indicated that the residual stresses scale with the *VED* and the samples with the same *VED* had similar residual stresses, see Fig. 8. Therefore, one way of increasing strain age cracking resistance could be to process with low *VED*. However, it must be kept in mind that the lack of fusion defects can form at low *VED* which might not be as easy to heal using hot isostatic pressing.
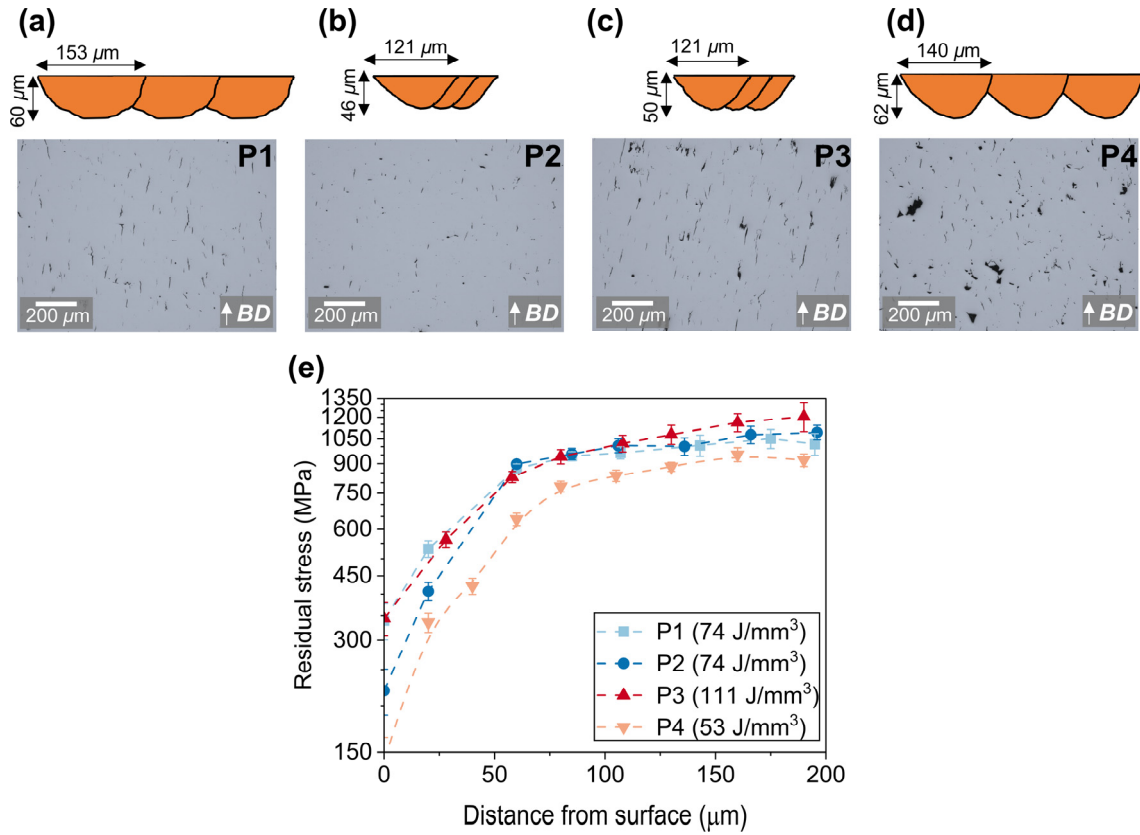
*Figure 8. Melt pool geometry and optical micrographs of samples built with parameters **(a)** P1 (74 J/mm³): P = 100 W, v = 500 mm/s, h = 0.09 mm, **(b)** P2 (74 J/mm³): P = 200 W, v = 3000 mm/s, h = 0.03 mm, **(c)** P3 (111 J/mm³): P = 300 W, v = 3000 mm/s, h = 0.03 mm, **(d)** P4 (53 J/mm³): P = 200 W, v = 1750 mm/s, h = 0.09 mm, **(e)** Depth profile of residual stress (along the BD), obtained using XRD and electrolytic polishing, for process parameters P1, P2, P3 and P4. BD = building direction [17].*

RQ2: How can novel scan strategies enable nearly defect-free processing of non-weldable Ni-base superalloy?

Paper I revealed that solidification cracking and residual stresses cannot be reduced just by optimizing laser power, speed, and hatch. This led to Paper II, where laser power, speed, and hatch were fixed while stripe width was varied. The stripe width has been varied from 5 to 0.2 mm. The reason for exploring stripe widths as low as 0.2 mm is to mimic point-like melting that could modify the thermal gradients and in turn the solidification cracking and the residual stresses. The optical micrographs and the crack density measurements revealed that stripe width had a profound effect on solidification cracking (Fig. 9). The cracking is found to increase as the stripe width is reduced from 5 to 1 mm. This is followed by a sharp decrease in crack density with a further reduction of stripe width from 1 to 0.2 mm. Melt pool analysis revealed that melt pool depth decreased with decreasing stripe width. This is shown to have a major effect on solidification structure and microstructure which was used to explain the cracking behavior. The solidification cracking was minimized when the solidification structure is nearly parallel to the build direction. This led to presence of highly textured microstructure with a lower fraction of high angle grain boundaries (HAGB).
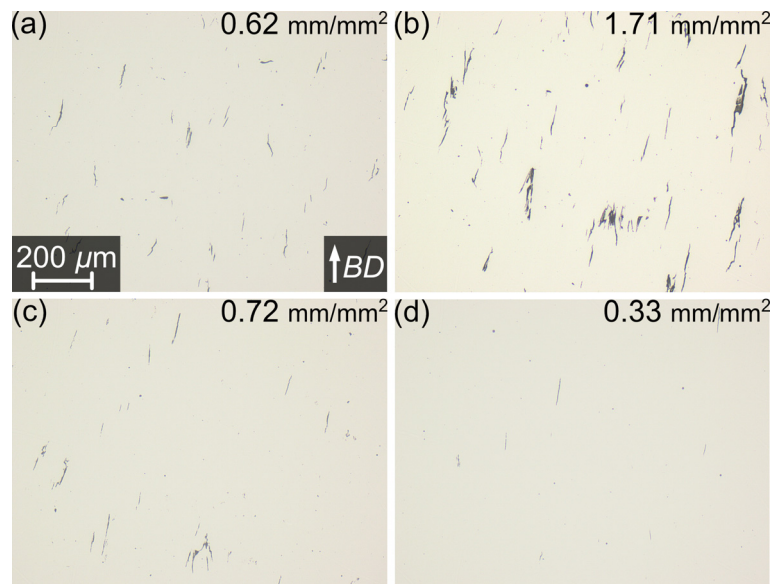

*Figure 9. OM images of the samples for selected stripe widths of **(a)** 5 mm, **(b)** 1 mm, **(c)** 0.5 mm, and **(d)** 0.2 mm. All the images have the same scale as shown in (a) and crack densities (in mm/mm²) are indicated in the top right corners.*

The residual stress measurements revealed that the residual stresses are impacted by stripe width (Fig. 10). The residual stresses first decrease as the stripe width reduces from 5 to 1 mm, this is then followed by a sharp increase in residual stresses for stripe width of 0.5 mm. This is followed by the lowest residual stresses obtained for the stripe width of 0.2 mm. The behavior of the residual stresses has been explained by two hypotheses. First, the reduction in residual stresses correlates well with the crack density for all the samples except 0.2 mm stripe width. An increase in crack density possibly leads to some relaxation and hence lower residual stresses. However, the 0.2 mm stripe width had lower crack density, and the low residual stress levels are explained by the increased re-melting that occurs due to the stripe overlap being 0.12 mm. Secondly, it was observed from ECCI that the dislocation density and arrangement were found to be affected by the stripe width (Fig. 11 and Table 2). It was observed that the dislocation density could be correlated with the residual stress behavior. The dislocation density is found to be higher for 0.7 and 0.5 mm relative to the others which explains the high residual stresses.
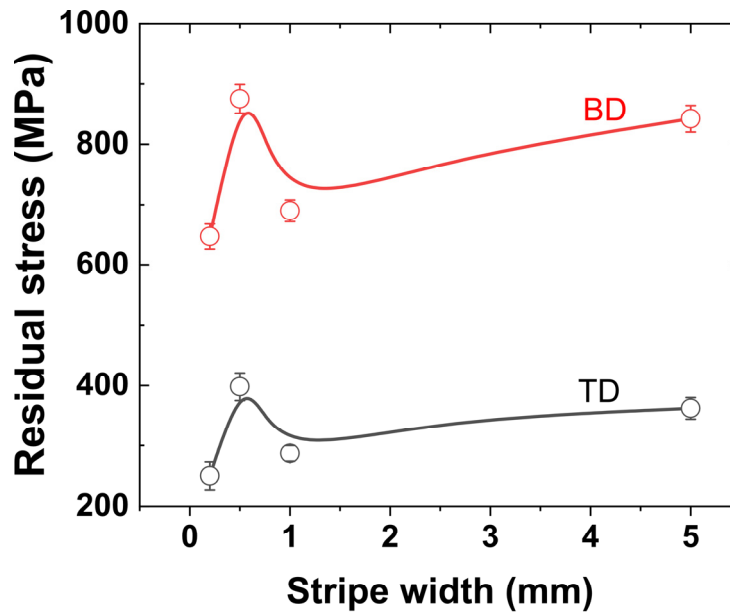

Figure 10. Variation of residual stress with stripe width of selected samples. BD and TD are residual stresses in the build direction and transverse direction, respectively. Error bars correspond to the standard deviation 2σ.
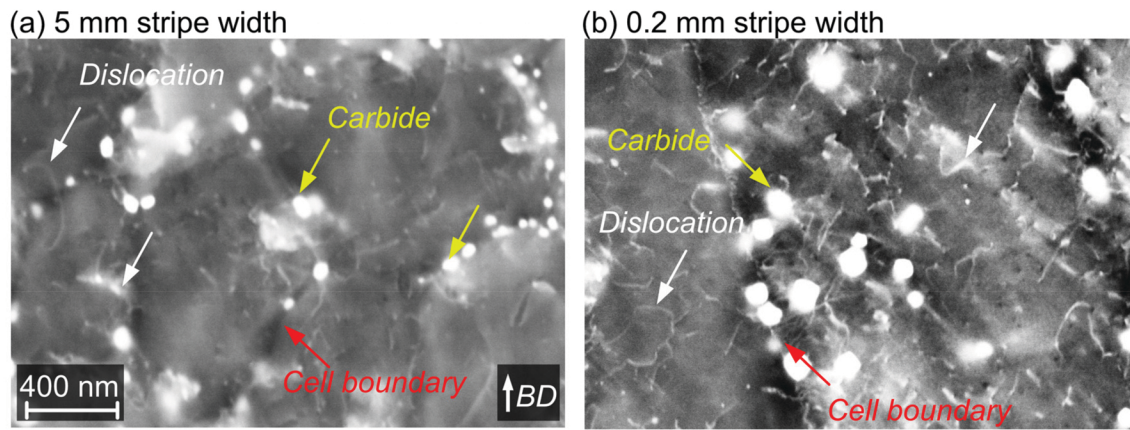
Figure 11. ECCI of samples manufactured with stripe widths of (a) 5 mm and (b) 0.2 mm.

Table 2. Dislocation density measurements for samples manufactured with different stripe widths.

Stripe width (mm)	5	2.5	1	0.7	0.5	0.2
Dislocation density ($\times 10^{14}$ m^{-2})	3.7	3.9	4.8	5.8	8.5	4.8

6. Conclusions

The following conclusions can be drawn from the work presented in this thesis:

RQ1: What is the impact of process parameters on microstructure and cracking in a non-weldable Ni-base superalloy?

- CM247LC samples processed with low *LED* (0.1 J/mm) and hatch spacing (0.03 mm) have the lowest crack density (0.74 mm/mm^2). Low *LED* causes shallower and narrower melt pools that coupled with low hatch spacing reduces the risk of lack of fusion.

- The micro-cracks observed in CM247LC had dendritic morphology and are confirmed to be solidification cracking. The absence of γ' precipitates confirmed by atom probe tomography also negates the strain age cracking argument.

- Residual stresses were affected by VED. The magnitude of residual stresses was proportional to the *VED*. Samples processed with completely different process parameters also had similar residual stresses. It is of high interest to minimize residual stresses to minimize strain age cracking, but there is a compromise required as a lack of fusion can form at low *VED*.

- The solidification cracking could not be eliminated through the process optimization involving laser power, speed, and hatch. Therefore, other strategies such as modified scan strategies or increased pre-heating can be explored.

RQ2: How can novel scan strategies enable defect-free processing of non-weldable Ni-base superalloy?

- The decrease in stripe width from 5 to 0.2 mm led to a reduction in the average melt pool depth by 28 %. However, the crack density first increased as the stripe width was reduced from 5 to 1 mm. This was followed by a sharp decrease as the stripe width was reduced to 0.2 mm. The variation in crack density is a combined effect of the changes in the solidification structure, microstructure, and mushy zone.

- Higher segregations of Hf and B were found in the grain boundaries of the samples processed with 0.2 mm stripe width when compared to the 5 mm stripe width. This is attributed to the increased re-melting that causes solute re-distribution.

- The average residual stress in the build direction decreased from 842 MPa to 690 MPa as the stripe width was reduced from 5 to 1 mm. However, there was a sharp peak at 875 MPa for the 0.5 mm stripe width followed by the lowest residual stresses of 647

MPa for the 0.2 mm stripe width. The variation between 5 and 0.5 mm stripe width is possibly caused due to the solidification cracking relieving the stresses. However, the re-melting is believed to have caused stress relief for the 0.2 mm stripe width.

Future work

From the results presented in this licentiate thesis, the following is the recommended future work:

- Further parameter optimization involving laser power, speed, and hatch spacing can be performed to further reduce the crack density. This can be done at low *LED* and low hatch spacing based on the results of Paper I.

- The point-like melting strategy shown in Paper II can be further developed. This strategy was realized by varying the stripe width for power, speed, and hatch optimized for 5 mm stripe width. However, dedicated process optimization can be performed along with heat treatments and high temperature testing.

- Other scan strategies such as scan rotation, re-melting, or laser post-exposure treatment can further be explored. The cracking, residual stresses, and unique microstructures obtained from such strategies can be of high interest.

- Previous research for other superalloys has indicated that dedicated heat treatment optimization is important for superalloys due to their sluggish recrystallization kinetics. Therefore, the impact of solution heat treatment and hot isostatic pressing with different parameters (say *VED*) can be of interest to study the recrystallization kinetics. Suitable samples can then be tested for high-temperature properties (like creep) and strain age cracking resistance.

- The impact of elements that act as grain boundary strengtheners (Hf, B, and Zr) on CM247LC is another interesting aspect. These elements have been known to segregate to grain boundaries and cause solidification cracking. At the same time, they are required for high temperature creep properties. Therefore, their impact on solidification cracking, strain age cracking, and creep properties should be explored.

Acknowledgements

References

[1]   Grand View Research, 3D Printing Market Size, Share & Trends Analysis Report By Component (Hardware, Software, Services), By Printer Type, By Technology, By Software, By Application, By Vertical, By Region, And Segment Forecasts, 2023 - 2030, 2021. https://www.grandviewresearch.com/industry-analysis/3d-printing-industry-analysis.

[2]   ISO/ASTM, ISO/ASTM 52911-1:2019, Additive manufacturing – Design – Part 1: Laser-based powder bed fusion of metals, 2019. https://www.iso.org/standard/72951.html.

[3]   O. Andersson, A. Graichen, H. Brodin, V. Navrotsky, Developing Additive Manufacturing Technology for Burner Repair, J. Eng. Gas Turbines Power 139 (2017) 1–9. https://doi.org/10.1115/1.4034235.

[4]   Siemens AG, Siemens and E.ON reach milestone with 3D-printed burner for SGT-700 gas turbine, PR2018090304PSEN (2018). https://press.siemens.com/global/en/pressrelease/siemens-and-eon-reach-milestone-3d-printed-burner-sgt-700-gas-turbine (accessed March 18, 2024).

[5]   M. Lindbäck, K. Frankolin, E. Tuneskog, B. Karlsson, L. Wang, Development and Validation Under Engine Operation Environment of Addtively Manufactured Hot Turbine Parts, 2023. https://doi.org/https://doi.org/10.1115/GT2023-103771.

[6]   I. Serrano-Munoz, T. Mishurova, T. Thiede, M. Sprengel, A. Kromm, N. Nadammal, G. Nolze, R. Saliwan-Neumann, A. Evans, G. Bruno, The residual stress in as-built Laser Powder Bed Fusion IN718 alloy as a consequence of the scanning strategy induced microstructure, Sci. Rep. 10 (2020) 1–15. https://doi.org/10.1038/s41598-020-71112-9.

[7]   A. Leicht, C.H. Yu, V. Luzin, U. Klement, E. Hryha, Effect of scan rotation on the microstructure development and mechanical properties of 316L parts produced by laser powder bed fusion, Mater. Charact. 163 (2020) 2–10. https://doi.org/10.1016/j.matchar.2020.110309.

[8]   P. Kontis, E. Chauvet, Z. Peng, J. He, A.K. da Silva, D. Raabe, C. Tassin, J.J. Blandin, S. Abed, R. Dendievel, B. Gault, G. Martin, Atomic-scale grain boundary engineering to overcome hot-cracking in additively-manufactured superalloys, Acta Mater. 177 (2019) 209–221. https://doi.org/10.1016/j.actamat.2019.07.041.

[9]   B. Wei, Z. Liu, B. Cao, B. Nong, Y. Zhang, Y. Ren, H. Zhou, S. Wei, Cracking inhibition of nano-TiC reinforced René 104 superalloy fabricated by selective laser melting, J. Alloys Compd. 881 (2021) 160413. https://doi.org/10.1016/j.jallcom.2021.160413.

[10]   M.C. Lam, S.C.V. Lim, H. Song, Y. Zhu, X. Wu, A. Huang, Scanning strategy induced cracking and anisotropic weakening in grain texture of additively manufactured superalloys, Addit. Manuf. 52 (2022) 102660. https://doi.org/10.1016/j.addma.2022.102660.

[11]   S. Kou, Welding metallurgy., 2. ed., Wiley, 2003. https://search.ebscohost.com/login.aspx?direct=true&db=cat07470a&AN=clc.ad7629d2.db86.42f7.a711.34443afdb233&site=eds-live&scope=site&authtype=guest&custid=s3911979&groupid=main&profile=eds.

[12]   A. Mostafaei, C. Zhao, Y. He, S. Reza Ghiaasiaan, B. Shi, S. Shao, N. Shamsaei, Z. Wu,

N. Kouraytem, T. Sun, J. Pauza, J. V. Gordon, B. Webler, N.D. Parab, M. Asherloo, Q. Guo, L. Chen, A.D. Rollett, Defects and anomalies in powder bed fusion metal additive manufacturing, Curr. Opin. Solid State Mater. Sci. 26 (2022) 100974. https://doi.org/10.1016/j.cossms.2021.100974.

[13] Y. Huang, T.G. Fleming, S.J. Clark, S. Marussi, K. Fezzaa, J. Thiyagalingam, C.L.A. Leung, P.D. Lee, Keyhole fluctuation and pore formation mechanisms during laser powder bed fusion additive manufacturing, Nat. Commun. 13 (2022) 1170. https://doi.org/10.1038/s41467-022-28694-x.

[14] C.T. Sims, N.S. Stoloff, W.C. Hagel, Superalloys II, Wiley, New York, 1987.

[15] M. Prager, C.S. Shira, Welding of Precipitation-Hardening Nickel-Base Alloys, Welding Research Council, 1968. https://books.google.se/books?id=rNoiHQAACAAJ.

[16] Y.T. Tang, C. Panwisawas, J.N. Ghoussoub, Y. Gong, J.W.G. Clark, A.A.N. Németh, D.G. McCartney, R.C. Reed, Alloys-by-design: Application to new superalloys for additive manufacturing, Acta Mater. 202 (2021) 417–436. https://doi.org/10.1016/j.actamat.2020.09.023.

[17] A. Fardan, A. Fazi, R.L. Peng, T. Mishurova, M. Thuvander, G. Bruno, H. Brodin, E. Hryha, Fine-Tuning Melt Pools and Microstructures: Taming Cracks in Powder Bed Fusion – Laser Beam of a non-weldable Ni-base Superalloy, Materialia (2024) 102059. https://doi.org/https://doi.org/10.1016/j.mtla.2024.102059.

[18] F. Schulz, K. Lindgren, J. Xu, E. Hryha, Gamma prime formation in nickel-based superalloy IN738LC manufactured by laser powder bed fusion, Mater. Today Commun. (2023) 107905. https://doi.org/10.1016/j.mtcomm.2023.107905.

[19] A.S. Shaikh, M. Rashidi, K. Minet-lallemand, K. Minet-lallemand, On as-built microstructure and necessity of solution treatment in additively manufactured Inconel 939, Powder Metall. (2022) 1–9. https://doi.org/10.1080/00325899.2022.2041787.

[20] Haynes International, HAYNES 282 Alloy Brochure, Kokomo, 2021.

[21] W. Huang, J. Yang, H. Yang, G. Jing, Z. Wang, X. Zeng, Heat treatment of Inconel 718 produced by selective laser melting: Microstructure and mechanical properties, Mater. Sci. Eng. A 750 (2019) 98–107. https://doi.org/10.1016/j.msea.2019.02.046.

[22] J.R. Miller, J.F.S. Markanday, S.M. Fairclough, G.J. Wise, C.M.F. Rae, L.R. Owen, D. Stapleton, N. D'Souza, P.A.J. Bagot, H.J. Stone, Gamma prime precipitation in as-deposited Ni-based superalloy IN713LC, Scr. Mater. 239 (2024) 115775. https://doi.org/10.1016/j.scriptamat.2023.115775.

[23] C. Körner, M. Ramsperger, C. Meid, D. Bürger, P. Wollgramm, M. Bartsch, G. Eggeler, Microstructure and Mechanical Properties of CMSX-4 Single Crystals Prepared by Additive Manufacturing, Metall. Mater. Trans. A Phys. Metall. Mater. Sci. 49 (2018) 3781–3792. https://doi.org/10.1007/s11661-018-4762-5.

[24] J. Xu, H. Gruber, R.L. Peng, J. Moverare, A novel γ'-strengthened nickel-based superalloy for laser powder bed fusion, Materials (Basel). 13 (2020) 1–12. https://doi.org/10.3390/ma13214930.

[25] N.J. Harrison, I. Todd, K. Mumtaz, Reduction of micro-cracking in nickel superalloys processed by Selective Laser Melting: A fundamental alloy design approach, Acta Mater. 94 (2015) 59–68. https://doi.org/10.1016/j.actamat.2015.04.035.

[26] Y. Zhao, Z. Ma, L. Yu, Y. Liu, New alloy design approach to inhibiting hot cracking in laser additive manufactured nickel-based superalloys, Acta Mater. 247 (2023) 118736. https://doi.org/10.1016/j.actamat.2023.118736.

[27] S. Kou, Weld Metal Solidification Cracking, in: Weld. Metall., 2002: pp. 263–300. https://doi.org/https://doi.org/10.1002/0471434027.ch11.

[28] J.N. DuPont, J.C. Lippold, S.D. Kiser, Welding Metallurgy and Weldability of Nickel-Base Alloys, Wiley Online Library, 2009. https://doi.org/10.1002/9780470500262.

[29] J.N. Ghoussoub, Y.T. Tang, C. Panwisawas, A. Németh, R.C. Reed, On the Influence of Alloy Chemistry and Processing Conditions on Additive Manufacturability of Ni-Based Superalloys, Springer International Publishing, 2020. https://doi.org/10.1007/978-3-030-51834-9_15.

[30] R. Engeli, T. Etter, S. Hövel, K. Wegener, Processability of different IN738LC powder batches by selective laser melting, J. Mater. Process. Technol. 229 (2016) 484–491. https://doi.org/10.1016/j.jmatprotec.2015.09.046.

[31] D. Grange, J.D. Bartout, B. Macquaire, C. Colin, Processing a non-weldable nickel-base superalloy by Selective Laser Melting: role of the shape and size of the melt pools on solidification cracking, Materialia 12 (2020). https://doi.org/10.1016/j.mtla.2020.100686.

[32] H. Gruber, E. Hryha, K. Lindgren, Y. Cao, M. Rashidi, L. Nyborg, The Effect of Boron and Zirconium on the Microcracking Susceptibility of IN-738LC Derivatives in Laser Powder Bed Fusion, Appl. Surf. Sci. 573 (2021) 151541. https://doi.org/10.1016/j.apsusc.2021.151541.

[33] L.N. Carter, M.M. Attallah, R.C. Reed, Laser powder bed fabrication of nickel-base superalloys: Influence of parameters; characterisation, quantification and mitigation of cracking, Proc. Int. Symp. Superalloys (2012) 577–586. https://doi.org/10.7449/2012/superalloys_2012_577_586.

[34] O. Adegoke, J. Andersson, H. Brodin, R. Pederson, Influence of laser powder bed fusion process parameters on voids, cracks, and microhardness of nickel-based superalloy alloy 247LC, Materials (Basel). 13 (2020) 1–23. https://doi.org/10.3390/MA13173770.

[35] B. Kumar, S. Sahu, D. Srinivasan, N.J. Balila, Influence of Heat Input on Solidification Cracking in Additively Manufactured CM247LC Ni-based Superalloy, Metall. Mater. Trans. A (2022). https://doi.org/10.1007/s11661-023-07027-7.

[36] S. Griffiths, H. Ghasemi Tabasi, T. Ivas, X. Maeder, A. De Luca, K. Zweiacker, R. Wróbel, J. Jhabvala, R.E. Logé, C. Leinenbach, Combining alloy and process modification for micro-crack mitigation in an additively manufactured Ni-base superalloy, Addit. Manuf. 36 (2020). https://doi.org/10.1016/j.addma.2020.101443.

[37] P. Kontis, H.A.M. Yusof, S. Pedrazzini, M. Danaie, K.L. Moore, P.A.J. Bagot, M.P. Moody, C.R.M. Grovenor, R.C. Reed, On the effect of boron on grain boundary character in a new polycrystalline superalloy, Acta Mater. 103 (2016) 688–699. https://doi.org/10.1016/J.ACTAMAT.2015.10.006.

[38] A. Després, S. Antonov, C. Mayer, C. Tassin, M. Veron, J.J. Blandin, P. Kontis, G. Martin, On the role of boron, carbon and zirconium on hot cracking and creep resistance of an additively manufactured polycrystalline superalloy, Materialia 19 (2021).

https://doi.org/10.1016/j.mtla.2021.101193.

[39]   J. Xu, P. Kontis, R.L. Peng, J. Moverare, Modelling of additive manufacturability of nickel-based superalloys for laser powder bed fusion, Acta Mater. 240 (2022) 118307. https://doi.org/10.1016/j.actamat.2022.118307.

[40]   J.N. Ghoussoub, Y.T. Tang, W.J.B. Dick-Cleland, A.A.N. Németh, Y. Gong, D.G. McCartney, A.C.F. Cocks, R.C. Reed, On the Influence of Alloy Composition on the Additive Manufacturability of Ni-Based Superalloys, Metall. Mater. Trans. A 53 (2022) 962–983. https://doi.org/10.1007/s11661-021-06568-z.

[41]   A. Jena, S.E. Atabay, A. Gontcharov, P. Lowden, M. Brochu, Laser powder bed fusion of a new high gamma prime Ni-based superalloy with improved weldability, Mater. Des. 208 (2021) 109895. https://doi.org/10.1016/j.matdes.2021.109895.

[42]   A.B. Gontcharov, P. Lowden, A. Jena, S. Kwon, M. Brochu, Weldability and properties of newly developed LW4280 high gamma prime nickel based superalloy for 3D am and repair of turbine engine components, Proc. ASME Turbo Expo 7 (2021) 1–10. https://doi.org/10.1115/GT2021-58851.

[43]   D. Grange, J.D. Bartout, B. Macquaire, C. Colin, Processing a non-weldable nickel-base superalloy by Selective Laser Melting: role of the shape and size of the melt pools on solidification cracking, Materialia 12 (2020). https://doi.org/10.1016/j.mtla.2020.100686.

[44]   M. Rappaz, A. Jacot, W.J. Boettinger, Last-stage solidification of alloys: Theoretical model of dendrite-arm and grain coalescence, Metall. Mater. Trans. A Phys. Metall. Mater. Sci. 34 A (2003) 467–479. https://doi.org/10.1007/s11661-003-0083-3.

[45]   Y. Chen, W. Wang, Y. Ou, D. Li, H. Chang, Y. Wu, R. Yang, Z. Zhai, C. Li, Effect of high preheating on the microstructure and mechanical properties of high gamma prime Ni-based superalloy manufactured by laser powder bed fusion, J. Alloys Compd. 960 (2023) 170598. https://doi.org/10.1016/j.jallcom.2023.170598.

[46]   W. Zhou, G. Zhu, R. Wang, C. Yang, Y. Tian, L. Zhang, A. Dong, D. Wang, D. Shu, B. Sun, Inhibition of cracking by grain boundary modification in a non-weldable nickel-based superalloy processed by laser powder bed fusion, Mater. Sci. Eng. A 791 (2020) 139745. https://doi.org/10.1016/j.msea.2020.139745.

[47]   E. Bassini, A. Sivo, P.A. Martelli, E. Rajczak, G. Marchese, F. Calignano, S. Biamino, D. Ugues, Effects of the solution and first aging treatment applied to as-built and post-HIP CM247 produced via laser powder bed fusion (LPBF), J. Alloys Compd. 905 (2022) 164213. https://doi.org/10.1016/j.jallcom.2022.164213.

[48]   J.U. Lee, Y.K. Kim, S.M. Seo, K.A. Lee, Effects of hot isostatic pressing treatment on the microstructure and tensile properties of Ni-based superalloy CM247LC manufactured by selective laser melting, Mater. Sci. Eng. A 841 (2022) 143083. https://doi.org/10.1016/j.msea.2022.143083.

[49]   S. Griffiths, H. Ghasemi-Tabasi, A. De Luca, J. Pado, S.S. Joglekar, J. Jhabvala, R.E. Logé, C. Leinenbach, Influence of Hf on the heat treatment response of additively manufactured Ni-base superalloy CM247LC, Mater. Charact. 171 (2021). https://doi.org/10.1016/j.matchar.2020.110815.

[50]   H. Hilal, R. Lancaster, D. Stapleton, G. Baxter, Investigating the influence of process

parameters on the structural integrity of an additively manufactured nickel-based superalloy, Metals (Basel). 9 (2019). https://doi.org/10.3390/met9111191.

[51]   S. Zaefferer, N.N. Elhami, Theory and application of electron channelling contrast imaging under controlled diffraction conditions, Acta Mater. 75 (2014) 20–50. https://doi.org/10.1016/j.actamat.2014.04.018.